Journal of Materials Chemistry A

ROYAL SOCIETY OF CHEMISTRY

COMMUNICATION

View Article Online
View Journal | View Issue

Cite this: *J. Mater. Chem. A*, 2020, **8**, 1059

Received 20th November 2019
Accepted 21st December 2019

DOI: 10.1039/c9ta12743g

rsc.li/materials-a

Promoting nitrogen photofixation over a periodic WS_2@TiO_2 nanoporous film†

Li Shi,‡[a] Zhao Li,‡[ab] Licheng Ju,[ab] Alejandro Carrasco-Pena,[c] Nina Orlovskaya,[cf] Haiqing Zhou[de] and Yang Yang*[abf]

Atmospheric nitrogen fixation using a photocatalytic system is a promising approach to produce ammonia. However, most of the recently explored photocatalysts for N_2 fixation are in the powder form, suffering from agglomeration and difficulty in the collection and leading to unsatisfactory conversion efficiency. Developing efficient film catalysts for N_2 photofixation under ambient conditions remains challenging. Herein, we report the efficient photofixation of N_2 over a periodic WS_2@TiO_2 nanoporous film, which is fabricated through a facile method that combines anodization, E-beam evaporation, and chemical vapor deposition (CVD). Oxygen vacancies are introduced into TiO_2 nanoporous films through Ar annealing treatment, which plays a vital role in N_2 adsorption and activation. The periodic WS_2@TiO_2 nanoporous film with an optimized WS_2 content shows highly efficient photocatalytic performance for N_2 fixation with an NH_3 evolution rate of 1.39 mmol g^{-1} h^{-1}, representing one of the state-of-the-art catalysts.

Introduction

Ammonia (NH_3) has received great attention because it serves as a hydrogen carrier and fuel in industry.[1] Furthermore, it is also the chemical molecule that plays a vital role in biological processes and sustains all living organisms by serving as building blocks for proteins.[1] Currently, the commercialized method for NH_3 synthesis is usually based on the Haber–Bosch process, which is performed under drastic conditions (20–40 MPa, 400–600 °C), consuming over 1% of the world's total energy supply, and simultaneously induces a large amount of CO_2 emission *via* fossil fuel reforming.[2] Converting solar energy into NH_3 using artificial photosynthesis systems has been regarded as a promising option to overcome the aforementioned problems by utilizing clean solar energy.[3]

Unfortunately, the obtained efficiency of photocatalytic nitrogen (N_2) fixation is far from satisfactory, which is severely limited by the poor absorption of N_2 on the photocatalysts and the high energy potential of intermediate products involved in the reactions.[4] The cleavage of the N≡N bond is very challenging because of its extremely high bonding energy (~941 kJ mol^{-1}), which is hard to be fully cleaved by the photogenerated electrons from the conduction band of photocatalysts.[5] The creation of oxygen vacancies on the photocatalysts has been demonstrated as an effective way to improve the photocatalytic N_2 fixation efficiency, as the oxygen vacancies can act as an electron trap center to capture and activate N_2 molecules, efficiently promoting the N≡N bond cleavage.[6] Recently, Li and co-workers have illustrated that the oxygen vacancies in BiOBr are capable of activating the adsorbed N_2 for NH_3 formation.[6] Likewise, the oxygen vacancies in TiO_2 have also been demonstrated for N_2 photoreduction.[7] Traditionally, the photocatalysts used for N_2 fixation are mostly made in the form of nanopowders, which may suffer from poor recyclability due to the catalyst aggregation and deactivation. The nanostructured film materials should have the inherent advantages over the powdered photocatalysts in terms of easy transportation and collection for recycling.[8] Moreover, the nanostructured films with periodic morphologies are beneficial for reducing the diffusion length and transport pathway of the photogenerated charge carriers.[9]

[a]*NanoScience Technology Center, University of Central Florida, 4000 Central Florida Blvd., Orlando, Florida, 32816, USA. E-mail: Yang.Yang@ucf.edu*

[b]*Department of Materials Science and Engineering, University of Central Florida, 4000 Central Florida Blvd., Orlando, Florida, 32816, USA*

[c]*Department of Mechanical and Aerospace Engineering, University of Central Florida, 4000 Central Florida Blvd., Orlando, Florida, 32816, USA*

[d]*Key Laboratory of Low-Dimensional Quantum Structures and Quantum Control of Ministry of Education, School of Physics and Electronics, Hunan Normal University, Changsha 410081, China*

[e]*Key Laboratory for Matter Microstructure and Function of Hunan Province, Hunan Normal University, Changsha 410081, China*

[f]*Energy Conversion and Propulsion Cluster, University of Central Florida, 4000 Central Florida Blvd., Orlando, Florida, 32816, USA*

† Electronic supplementary information (ESI) available. See DOI: 10.1039/c9ta12743g

‡ These authors contributed equally to this work.

TiO_2 is the most investigated semiconductor photocatalyst due to its good activity and stability; however, it can hardly achieve the favorable charge-carrier separation because of its exciton binding energy barrier.[10] Thus, the rational design of TiO_2-based heterostructures has been intensively pursued to facilitate the charge separation of TiO_2 by separately transferring photogenerated electron–hole pairs to opposite sites of the heterojunction.[11] Semiconducting 2H-phase tungsten disulfide (WS_2) has achieved particular attention as it possesses suitable electronic band positions as compared to TiO_2, which enables TiO_2/WS_2 to form a type-II heterojunction with merits of improved separation efficiency of photogenerated charge carriers for the enhanced photocatalytic activity.[12] 2H-WS_2 has also been demonstrated as an effective photosensitizer for TiO_2 to achieve visible light photocatalysis due to its narrow bandgap.[13] However, similar to other powdered photocatalysts, the synthesis of the TiO_2/WS_2 composite is based on a solution-processed method, which would lead to materials agglomeration due to high surface energy. Therefore, exploring the synthetic method of the nanostructured WS_2/TiO_2 film catalysts with properly controlled geometry, size and distribution is in high demand.

Herein, we illustrate a rationally designed route to fabricate periodic WS_2@TiO_2 nanoporous films (NFs) by a facile method that combines anodization, E-beam evaporation, and chemical vapor deposition (CVD). As a consequence, nanoscale few-layer WS_2 flakes were individually deposited inside the nanopores of the periodic TiO_2 film. Oxygen vacancies were also intentionally introduced into the heterostructured WS_2@TiO_2 NFs to improve the photocatalytic conversion of N_2 to NH_3, which is due to efficient N_2 activation on the defective surfaces. The periodic WS_2@TiO_2 NFs with an optimized WS_2 content exhibit a significantly improved photocatalytic N_2 fixation performance with an NH_3 evolution rate of 1.39 mmol g^{-1} h^{-1}, due to the enhanced separation efficiency and prolonged lifetime of charge carriers.

Results and discussion

The schematic illustration of a synthetic procedure for the periodic WS_2@TiO_2 NFs is shown in Fig. 1a. First of all, the periodic TiO_2 NFs were fabricated by Ti anodization,[14] followed by thermal annealing under an Ar atmosphere. The morphology of the as-prepared TiO_2 NFs was investigated by scanning electron microscopy (SEM), showing honeycomb-like shape with an average pore size of 60 nm and thickness of 110 nm (Fig. 1b and c). Then, the W metal layers with different thicknesses of 10 nm, 20 nm, and 30 nm were deposited on the as-prepared TiO_2 NFs by E-beam evaporation. The SEM observation shows that the W layers have been conformally coated on the TiO_2 NFs as observed from the obvious wall thickening (increased from 10 nm to 20 nm, 30 nm, and 40 nm, respectively, after the W deposition, Fig. 1d, e, and S1†). The conformal W layer coating is also confirmed by the inner wall thickening of W@TiO_2 NFs as compared to the pristine TiO_2 NFs (Fig. 1e and S1†). Finally, chemical vapor deposition (CVD) was employed to convert W to WS_2 using a Na_2S and S mixture as an S-source, forming the periodic WS_2@TiO_2 NFs (abbreviated as nWS_2@TiO_2, *n* represents the W layer thickness, which is 10 nm, 20 nm, and 30 nm, respectively).

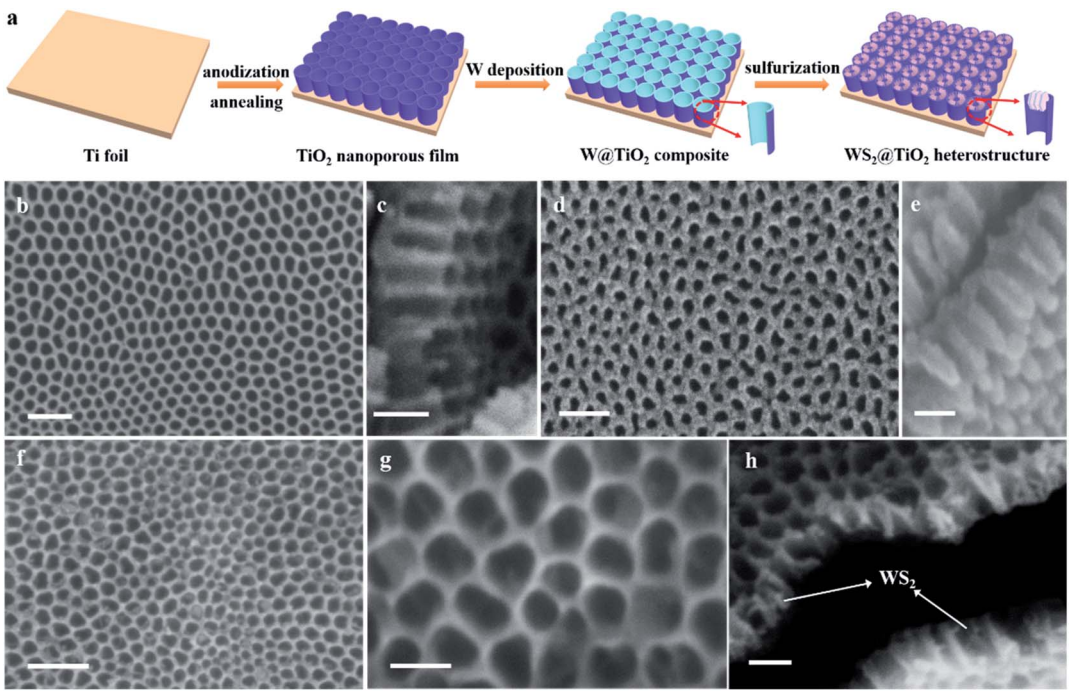

Fig. 1 (a) Schematic illustration of the WS_2@TiO_2 fabrication. SEM images of (b and c) TiO_2; (d and e) 20 nm W@TiO_2; (f–h) 20WS_2@TiO_2. Scale bars: (b) 200 nm, (c) 100 nm, (d) 200 nm, (e) 100 nm, (f) 200 nm, and (g and h) 100 nm.

The top-view SEM images of $20WS_2@TiO_2$ (Fig. 1f and g) show that the periodic TiO_2 nanopores are filled with WS_2 nanoflakes after CVD sulfurization treatment. The cross-sectional SEM image of $20WS_2@TiO_2$ (Fig. 1h) further confirms the formation of WS_2 nanoflakes inside the TiO_2 nanopores. Moreover, the WS_2 nanoflakes contact well with the inner wall of TiO_2 nanopores, resulting in the formation of the Schottky junction to facilitate the charge carrier transfer and separation. In addition, $10WS_2@TiO_2$ and $30WS_2@TiO_2$ show a similar morphology to $20WS_2@TiO_2$. The amount of WS_2 formed inside the TiO_2 nanopores increases with Mo thickness (Fig. S2†).

The transmission electron microscopy (TEM) image of $20WS_2@TiO_2$ (Fig. 2a) reveals that the WS_2 nanoflakes are grown inside the TiO_2 nanopores with a 3D laminated structure, which is consistent with the SEM observation. The high-resolution TEM (HR-TEM) image (Fig. 2b) exhibits lattice fringes of 0.35 nm and 0.62 nm, well in line with the (101) anatase TiO_2 and (002) WS_2 crystallographic planes, respectively.[15] The cross-sectional TEM and high angle annular dark-field (HAADF) scanning transmission electron microscopy (STEM) images of $20WS_2@TiO_2$ (Fig. 2c and d) further confirm that 3D laminated WS_2 is grown inside the TiO_2 nanopores, consistent with the SEM observation. During the CVD sulfurization process, the S stream derived from the Na_2S and S mixture reaches the surface of the TiO_2 NFs followed by diffusing gradually into the TiO_2 nanopores. The conversion from W to WS_2 occurs almost simultaneously upon S reaching the W surface. The TiO_2 nanopores provide the space-confined reaction vessel for W and S, and eventually, nanoscale laminated WS_2 is grown inside the TiO_2 nanopores. In sharp contrast, when using a flat TiO_2 film as a substrate to deposit WS_2, much larger WS_2 flakes with an aggregated architecture were obtained, confirming the significant contribution made by using the periodic TiO_2 NFs to suppress the overgrowth of WS_2 (Fig. S3†).

The phase composition of $WS_2@TiO_2$ was investigated by X-ray diffraction (XRD). As shown in Fig. 3a, the as-prepared TiO_2 NFs display the diffraction peaks of the Ti substrate and anatase TiO_2. As for $WS_2@TiO_2$, three additional weak and broad diffraction peaks at 14.0°, 33.2°, and 58.6° were observed, corresponding to the (002), (100) and (110) planes of the hexagonal 2H-WS_2 (JCPDS card no. 84-1398) respectively.[15a] The observed broad and asymmetric WS_2 (100) and (110) peaks indicate the formation of nanosized crystals with ultrathin thickness.[15a] The Raman spectra of $WS_2@TiO_2$ and TiO_2 NFs (Fig. 3b) show a typical peak located at 392.6 cm^{-1}, which is assigned to the B_{1g} mode of anatase TiO_2.[9b] As for the $WS_2@TiO_2$ NFs, two additional characteristic Raman peaks located at 353.1 and 417.1 cm^{-1} are observed, ascribed to the in-plane E^1_{2g} and the out-of-plane A_{1g} vibrational modes of the 2H-WS_2 phase, respectively.[16] The intensity ratios of E^1_{2g}/A_{1g} are 1.45 for $10WS_2@TiO_2$, 1.21 for $20WS_2@TiO_2$ and 1.12 for $30WS_2@TiO_2$, indicating the exfoliated WS_2 nanosheets.[17] No other phase impurities such as metallic W or its oxide can be detected from XRD and Raman spectroscopy, indicating a complete conversion from W to WS_2 after CVD sulfurization.

The chemical states and compositions of the samples were characterized by X-ray photoelectron spectroscopy (XPS). The high-resolution Ti 2p spectra (Fig. 3c) show two peaks at binding energies of 465.1 eV and 459.3 eV, corresponding to $2p_{1/2}$ and $2p_{3/2}$ of Ti^{4+}, respectively.[9b] The periodic TiO_2 NFs contain oxygen vacancies, which can be proved by O 1s spectra. The O 1s spectra of TiO_2 (Fig. 3d) can be fitted into three peaks centered at 533.6 eV, 532.3 eV, and 531.1 eV, which are attributed to the surface-adsorbed OH group, O-vacancy, and O-lattice, respectively.[18] The formation of oxygen vacancies in the TiO_2 NFs is due to the annealing treatment under an Ar atmosphere (see Experimental details). The existence of oxygen vacancies in the TiO_2 NFs can also be evidenced by the UV-vis absorption spectrum (Fig. S4†), which shows a strong light absorption tail in the visible light region.[19] The $WS_2@TiO_2$ NFs show similar O 1s peaks to bare TiO_2 NFs, indicating that the oxygen vacancies remain in the $WS_2@TiO_2$ NFs after sulfurization. Fig. S5† shows the high-resolution XPS spectra of W and S, respectively. The peaks are observed at binding energies of 38.0 eV, 34.7 eV, and 32.5 eV, illustrating the presence of W(IV) in WS_2.[20] The S 2p spectra show two strong peaks centered at binding energies of 163.4 eV and 162.2 eV, which are assigned to the S^{2-} in WS_2.[20] The XPS spectra of the air-annealed TiO_2 NFs were also recorded as shown in Fig. S6.† It is obvious that the content of oxygen vacancies in the air-annealed TiO_2 NFs dramatically decreases as compared to the Ar-annealed TiO_2 NFs (Fig. 3d). The formation of oxygen vacancies in the Ar-annealed TiO_2 NFs is due to the fact that the surface of TiO_2 NFs is unsaturated in the Ar-atmosphere. The air-annealed TiO_2 NFs show less amount of oxygen vacancies because the unsaturated surface of TiO_2 NFs would be compensated by the oxygen gas when the sample was heated in the air.

Photocatalytic N_2 reduction was conducted in a single-compartment cell with TiO_2 and $WS_2@TiO_2$ NFs immersed in the water/Na_2SO_3 solution with continuous N_2 bubbling under AM 1.5G irradiation. The indophenol blue method was used to quantitatively determine the produced NH_3, and the calibration curves of the relationship between the

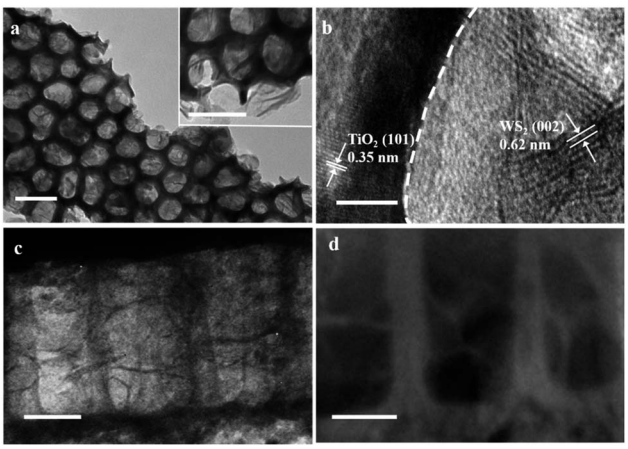

Fig. 2 (a) TEM images of $20WS_2@TiO_2$; (b) HRTEM image of $20WS_2@TiO_2$; (c) cross-sectional TEM image of $20WS_2@TiO_2$; (d) cross-sectional STEM image of $20WS_2@TiO_2$. Scale bars: (a) 100 nm, (b) 5 nm, (c) 50 nm, and (d) 50 nm.

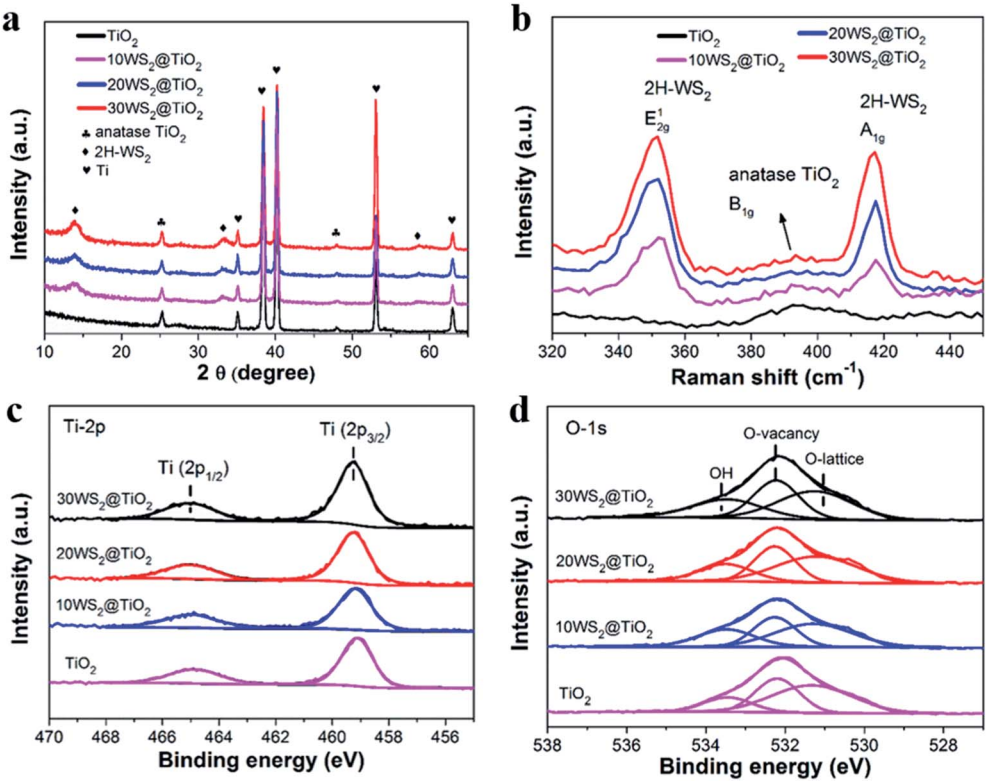

Fig. 3 (a) XRD patterns, (b) Raman spectra, and (c) high-resolution Ti XPS and (d) high-resolution O XPS spectra of samples.

concentration of NH^{4+} and absorbance were obtained (Fig. S7†). Fig. 4a shows the time-dependent NH_3 production over different samples. It can be seen that all the samples show photocatalytic performance for NH_3 production, and the amount of NH_3 increases almost linearly along with reaction time. In comparison with the bare TiO_2 NFs, the N_2 photofixation activities of the WS_2@TiO_2 NFs are greatly boosted to 0.13 μmol h^{-1} (*ca.* 1.39 mmol g^{-1} h^{-1}) in the 20WS_2@TiO_2 NFs. This photocatalytic N_2 fixation efficiency obtained by 20WS_2@TiO_2 is comparable to the state-of-the-art photocatalysts for N_2 reduction (Table S1†).[6,8a,8c,8d,21] The control experiment carried out by using aprotic solvent CH_3CN instead of water as a reaction solution shows no photocatalytic activity, suggesting that the proton source for NH_3 evolution originates from the water. The photocatalytic performance of 20WS_2/flat TiO_2 was evaluated (Fig. S8†), which shows lower activity than 20WS_2@TiO_2 NFs, demonstrating the advantages of the porous structure for photocatalysis. Under visible light irradiation, no detectable activity was observed over 20WS_2@TiO_2 NFs, indicating that the excitation of TiO_2 is necessary for NH_3 evolution (Fig. S9†). In pure water, the dramatically decreased activity was observed (Fig. S10†), indicating that the sacrificial agent plays a dominant role in trapping photogenerated holes, thus promoting the photocatalytic activity. The 20WS_2@TiO_2 NFs also exhibit good stability for photocatalytic N_2 fixation, with no obvious change in activity after four successive cycles (Fig. 4b). After the photocatalytic test, the 20WS_2@TiO_2 NFs show no obvious change of morphology and composition, as revealed by SEM and energy-dispersive spectroscopy (EDS) analysis (Fig. S11 and S12†). Inductively coupled plasma mass spectrometry (ICP-MS) of 20WS_2@TiO_2 before and after the reaction was performed. The weight ratio of W in 20WS_2@TiO_2 is 38.6%, while it slightly decreased to 36.5% after four successive cycles.

In order to track the N-related functional groups on the 20WS_2@TiO_2 surface during the N_2 fixation, *in situ* diffuse reflectance infrared Fourier transform spectroscopy (DRFTIRS) was performed. It can be seen that some bands gradually increased with the light irradiation time from 0 to 3 h (Fig. S13†). The sharp peak at 1415 cm^{-1} and weak peaks at 1736 cm^{-1} and 2807 cm^{-1} can readily be attributed to surface NH^{4+} species.[6] Furthermore, the peaks at 3040 cm^{-1} and 3142 cm^{-1} are assigned to the adsorbed H_2O and N–H stretching vibrations.[6,21b] The DRFTIRS results indicate that the 20WS_2@TiO_2 NFs can facilitate the activation of the N≡N bond until it is cleaved to NH^{4+} in the final step. As we knew, N_2 is difficult to be reduced directly under ambient conditions, due to its strong nonpolar N≡N bond. The oxygen vacancy on the surface of TiO_2 contributes to the photocatalytic N_2 reduction by acting as a binding site for N_2 activation.[22] The mechanism for the N_2 photofixation on the surface oxygen vacancy of TiO_2 is presented in Fig. S14,† in which the adsorbed N_2 can be converted to NH_3 *via* multiple reaction steps of proton-coupled hydrogenations on TiO_2.[8a] In order to demonstrate the importance of oxygen vacancies in photocatalytic N_2 fixation, the activities of the periodic TiO_2 NFs without surface oxygen

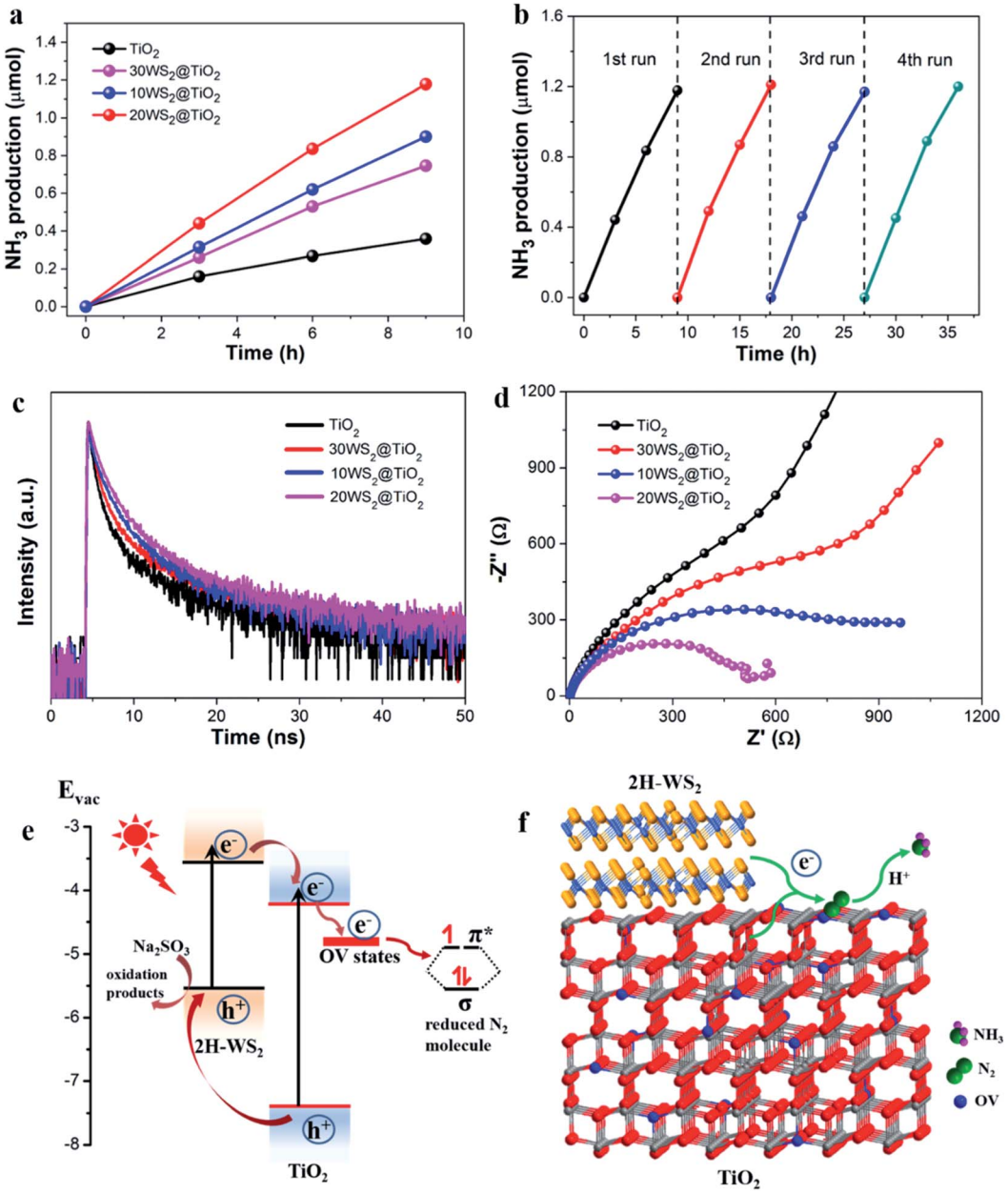

Fig. 4 (a) Time-dependent NH_3 evolution over various films. (b) Recycling test of $20WS_2@TiO_2$ for photocatalytic NH_3 evolution. (c) Decay time measurement and (d) Nyquist plots of various films. (e) Schematic illustrating the electron generation and transfer for N_2 reduction processes with $WS_2@TiO_2$. (f) Artistic illustration of the efficient N_2 photofixation. OV refers to oxygen vacancies.

vacancies were evaluated. The periodic TiO_2 NFs without surface oxygen vacancies were prepared *via* annealing the anodized TiO_2 NFs in the air at 450 °C. The air-annealed TiO_2 NFs show a similar morphology to the defective Ar-annealed TiO_2 NFs; however, their light absorption in the visible region is greatly weakened, due to the lack of oxygen vacancies (Fig. S4 and S15†). As expected, the air-annealed TiO_2 NFs show much lower activity than the Ar-annealed TiO_2 NFs, suggesting the critical role of oxygen vacancies in N_2 fixation (Fig. S16†).

The $WS_2@TiO_2$ NFs show higher photocatalytic performance for N_2 fixation than the bare TiO_2. The mechanism behind the functions of the heterostructures is further investigated. Due to the well-matched energy levels between WS_2 and TiO_2, a type II heterojunction can be formed in $WS_2@TiO_2$, resulting in enhanced charge-carrier separation and transfer.[12a] In order to prove this assumption, time-resolved PL decay and electrochemical impedance spectroscopy (EIS) measurements were performed. As shown in Fig. 4c, the decay curves support the triexponential fitting model and indicate a prolonged lifetime from 3.51 ns of TiO_2 to 4.72 ns of $30WS_2@TiO_2$, 5.31 ns of $10WS_2@TiO_2$ and 6.16 ns of $20WS_2@TiO_2$. The increased fluorescence lifetime suggests the suppressed recombination of the photogenerated charge carriers and the improved separation of electron–hole pairs in the $WS_2@TiO_2$ NFs.

Fig. 4d shows the Nyquist plots of TiO_2 and WS_2@TiO_2 NFs. The diameter of the semicircle in the Nyquist plots provides the information on the electron transfer resistance, which indicates the electron transfer kinetics.[23] The diameter of the semicircle follows the order TiO_2 > $30WS_2$@TiO_2 > $10WS_2$@TiO_2 > $20WS_2$@TiO_2. The smallest diameter is found for the curve of $20WS_2$@TiO_2, indicating a decreased charge-transfer resistance in $20WS_2$@TiO_2. The EIS results indicate the formation of the heterostructure assisted in the separation and transfer of photogenerated charge carriers. The inhibited surface recombination in WS_2@TiO_2 is further proved by the open-circuit potential (OCP) decay transient analysis. The OCP decay gives information about the surface charge recombination of the electrodes. Fig. S17† exhibits the normalized transient decay profiles of OCP in the bare TiO_2 and WS_2@TiO_2 NFs after interrupting the light illumination in H_2O/Na_2SO_3 electrolyte. The transient OCP curves of WS_2@TiO_2 show a much slower decay than the bare TiO_2, which is ascribed to the trapped holes being quickly scavenged by surface absorbed Na_2SO_3. Thus the accumulated electrons in the WS_2@TiO_2 electrodes have a longer survival time, contributing to the activation of the adsorbed N_2 since the fixation of N_2 is a multi-electron process (Fig. S14†).[6]

A N_2 photofixation mechanism over WS_2@TiO_2 (Fig. 4e and f) was proposed based on the above discussion. Upon AM 1.5G light illumination, electron–hole pairs are generated in both WS_2 and TiO_2. A type II band alignment forms between WS_2 and TiO_2 due to the well-matched band positions. The photo-excited electrons from the conduction band of WS_2 transfer to TiO_2 across the WS_2/TiO_2 interfaces. Subsequently, the electrons accumulated on the conduction band of TiO_2 will be trapped by oxygen vacancy states in TiO_2 and then injected into the empty antibonding orbitals (π^*) of the N_2 molecules, eventually leading to the formation of NH_3. Na_2SO_3 acts as an electron donor to consume the holes. The separation of the photogenerated charge carriers is facilitated by the increase of the WS_2 content in WS_2@TiO_2, leading to the improved photocatalytic N_2 fixation. However, a further increase in the WS_2 content ($30WS_2$@TiO_2) leads to a reduced light reception area (shading effect). In this case, some photogenerated charges on WS_2 tend to recombine instead of transferring to the adjacent TiO_2, leading to a decreased separation efficiency of electron–hole pairs.

Conclusion

In summary, periodic WS_2@TiO_2 NFs were synthesized by a facile method that combines anodization, E-beam evaporation and CVD. The TiO_2 nanopores provide the space-confined reaction vessel for W and S, beneficial for the conformal growth of nanoscale laminated WS_2 nanoflakes. The photocatalytic conversion of N_2 to NH_3 was achieved over the WS_2@TiO_2 films at room temperature and atmospheric pressure. Oxygen vacancies were introduced in TiO_2 through post-annealing in an Ar-atmosphere, which plays a vital role in photocatalytic N_2 fixation. The WS_2@TiO_2 film with an optimized WS_2 content (20 nm W) shows significantly improved photocatalytic performance compared to the bare TiO_2, reaching the NH_3 evolution rate as high as 0.13 μmol h^{-1} (*ca.* 1.39 mmol g^{-1} h^{-1}), due to the enhanced separation efficiency and prolonged lifetime of charge carriers. The catalyst design strategy developed in this work can be used for other solar energy conversion applications *via* altering the materials composition.

Conflicts of interest

There are no conflicts to declare.

Acknowledgements

This work was supported by the National Science Foundation under grant no. CMMI-1851674 and the startup grant from the University of Central Florida. L. S. acknowledges the financial support from the Preeminent Postdoctoral Program (P3) at the University of Central Florida. The XPS analysis performed by H. Z. was partially supported by Science and Technology Innovation Platform no. 2018RS3070 and Hundred Youth Talents Programs of Hunan Province, the 'XiaoXiang Scholar' Talents Foundation of Hunan Normal University in Changsha, P. R. China.

References

1 X. Chen, N. Li, Z. Kong, W.-J. Ong and X. Zhao, *Mater. Horiz.*, 2018, **5**, 9–27.
2 T. Kandemir, M. E. Schuster, A. Senyshyn, M. Behrens and R. Schlogl, *Angew. Chem., Int. Ed.*, 2013, **52**, 12723–12726.
3 (*a*) L. Li, Y. Wang, S. Vanka, X. Mu, Z. Mi and C. J. Li, *Angew. Chem., Int. Ed.*, 2017, **56**, 8701–8705; (*b*) S. Hu, X. Chen, Q. Li, F. Li, Z. Fan, H. Wang, Y. Wang, B. Zheng and G. Wu, *Appl. Catal., B*, 2017, **201**, 58–69.
4 H. Li, J. Li, Z. Ai, F. Jia and L. Zhang, *Angew. Chem., Int. Ed.*, 2018, **57**, 122–138.
5 S. Wang, X. Hai, X. Ding, K. Chang, Y. Xiang, X. Meng, Z. Yang, H. Chen and J. Ye, *Adv. Mater.*, 2017, **29**, 1701774.
6 H. Li, J. Shang, Z. Ai and L. Zhang, *J. Am. Chem. Soc.*, 2015, **137**, 6393–6399.
7 H. Hirakawa, M. Hashimoto, Y. Shiraishi and T. Hirai, *J. Am. Chem. Soc.*, 2017, **139**, 10929–10936.
8 (*a*) C. Li, T. Wang, Z. J. Zhao, W. Yang, J. F. Li, A. Li, Z. Yang, G. A. Ozin and J. Gong, *Angew. Chem., Int. Ed.*, 2018, **57**, 5278–5282; (*b*) T. Oshikiri, K. Ueno and H. Misawa, *Angew. Chem., Int. Ed.*, 2014, **53**, 9802–9805; (*c*) T. Oshikiri, K. Ueno and H. Misawa, *Angew. Chem., Int. Ed.*, 2016, **55**, 3942–3946; (*d*) M. Ali, F. Zhou, K. Chen, C. Kotzur, C. Xiao, L. Bourgeois, X. Zhang and D. R. MacFarlane, *Nat. Commun.*, 2016, **7**, 11335.
9 (*a*) L. Shi, W. Zhou, Z. Li, S. Koul, A. Kushima and Y. Yang, *ACS Nano*, 2018, **12**, 6335–6342; (*b*) L. Shi, Z. Li, T. D. Dao, T. Nagao and Y. Yang, *J. Mater. Chem. A*, 2018, **6**, 12978–12984.
10 J. Schneider, M. Matsuoka, M. Takeuchi, J. Zhang, Y. Horiuchi, M. Anpo and D. W. Bahnemann, *Chem. Rev.*, 2014, **114**, 9919–9986.

11 J. Low, J. Yu, M. Jaroniec, S. Wageh and A. A. Al-Ghamdi, *Adv. Mater.*, 2017, **29**, 1601694.
12 (*a*) B. Mahler, V. Hoepfner, K. Liao and G. A. Ozin, *J. Am. Chem. Soc.*, 2014, **136**, 14121–14127; (*b*) W. Ho, J. C. Yu, J. Lin, J. Yu and P. Li, *Langmuir*, 2004, **20**, 5865–5869.
13 (*a*) D. Jing and L. Guo, *Catal. Commun.*, 2007, **8**, 795–799; (*b*) L. Zheng, W. Zhang and X. Xiao, *Korean J. Chem. Eng.*, 2015, **33**, 107–113.
14 J. E. Yoo, K. Lee, M. Altomare, E. Selli and P. Schmuki, *Angew. Chem., Int. Ed.*, 2013, **52**, 7514–7517.
15 (*a*) X. Zeng, Z. Ding, C. Ma, L. Wu, J. Liu, L. Chen, D. G. Ivey and W. Wei, *ACS Appl. Mater. Interfaces*, 2016, **8**, 18841–18848; (*b*) Z. Li, L. Shi, D. Franklin, S. Koul, A. Kushima and Y. Yang, *Nano Energy*, 2018, **51**, 400–407.
16 F. Raza, D. Yim, J. H. Park, H. I. Kim, S. J. Jeon and J. H. Kim, *J. Am. Chem. Soc.*, 2017, **139**, 14767–14774.
17 Y. Yang, H. Fei, G. Ruan, Y. Li and J. M. Tour, *Adv. Funct. Mater.*, 2015, **25**, 6199–6204.
18 H. Tan, Z. Zhao, W. B. Zhu, E. N. Coker, B. Li, M. Zheng, W. Yu, H. Fan and Z. Sun, *ACS Appl. Mater. Interfaces*, 2014, **6**, 19184–19190.
19 L. Hou, M. Zhang, Z. Guan, Q. Li and J. Yang, *Appl. Surf. Sci.*, 2018, **428**, 640–647.
20 Y. Yan, B. Xia, N. Li, Z. Xu, A. Fisher and X. Wang, *J. Mater. Chem. A*, 2015, **3**, 131–135.
21 (*a*) A. Banerjee, B. D. Yuhas, E. A. Margulies, Y. Zhang, Y. Shim, M. R. Wasielewski and M. G. Kanatzidis, *J. Am. Chem. Soc.*, 2015, **137**, 2030–2034; (*b*) Y. Zhao, Y. Zhao, G. I. N. Waterhouse, L. Zheng, X. Cao, F. Teng, L. Z. Wu, C. H. Tung, D. O'Hare and T. Zhang, *Adv. Mater.*, 2017, **29**, 1703828.
22 J. Yang, Y. Guo, R. Jiang, F. Qin, H. Zhang, W. Lu, J. Wang and J. C. Yu, *J. Am. Chem. Soc.*, 2018, **140**, 8497–8508.
23 L. Shi, K. Chang, H. Zhang, X. Hai, L. Yang, T. Wang and J. Ye, *Small*, 2016, **12**, 4431–4439.